

Assimilation of Middepth Velocities from Argo Floats in the Western South China Sea

PINQIANG WANG

College of Meteorology and Oceanography, National University of Defense Technology, Changsha, China

WEIMIN ZHANG

College of Meteorology and Oceanography, National University of Defense Technology, and Laboratory of Software Engineering for Complex Systems, Changsha, China

HUIZAN WANG AND HAIJIN DAI

College of Meteorology and Oceanography, National University of Defense Technology, Changsha, China

XIAOHUI WANG

College of Meteorology and Oceanography, National University of Defense Technology, Changsha, China, and Delft Institute of Applied Mathematics, Delft University of Technology, Delft, Netherlands

(Manuscript received 9 January 2019, in final form 17 October 2019)

ABSTRACT

Previous studies are mainly limited to temperature and salinity (T/S) profiling data assimilation, while data assimilation based on Argo float trajectory information has received less research focus. In this study, a new method was proposed to assimilate Argo trajectory data: the middepth (indicates the parking depth of Argo floats in this study, ~ 1200 m) velocities are estimated from Argo trajectories and subsequently assimilated into the Regional Ocean Model System (ROMS) using four-dimensional variational data assimilation (4DVAR) method. This method can avoid a complicated float trajectory model in direct position assimilation. The 2-month assimilation experiments in South China Sea (SCS) showed that this proposed method can effectively assimilate Argo trajectory information into the model and improve middepth velocity field by adjusting the unbalanced component in the velocity increments. The assimilation of the Argo trajectory-derived middepth velocity with other observations (satellite observations and T/S profiling data) together yielded the best performance, and the velocity fields at the float parking depth are more consistent with the Argo float trajectories. In addition, this method will not decrease the assimilation performance of other observations [i.e., sea level anomaly (SLA), sea surface temperature (SST), and T/S profiles], which is indicative of compatibility with other observations in the 4DVAR assimilation system.

1. Introduction

As the largest marginal sea in the west Pacific Ocean, the South China Sea (SCS) is strongly influenced by the wind, which has intraseasonal variations. As a result, the upper layer circulation of the SCS is characterized by anticyclonic circulation in the southern SCS, cyclonic circulation in the northern SCS during summer and cyclonic circulation during winter because of the wind

direction reversal (Wyrтки 1961; Hu et al. 2000; Liu et al. 2008). The current structures below 500 m are poorly understood and less studied than the upper circulation due to the lack of observations. The intermediate circulation studies are mainly based on the diagnosis of hydrography data (Chu and Li 2000), numerical simulations (Chao et al. 1996; Yuan 2012) and some in situ observations (Liao et al. 2005). The circulation in the middle layer of the SCS appears as an overall anticyclonic circulation, driven by the outflow from the SCS to the Pacific Ocean in the Luzon Strait (Yuan 2012).

Corresponding author: W. Zhang, wmzhang104@139.com

DOI: 10.1175/JTECH-D-18-0233.1

© 2020 American Meteorological Society. For information regarding reuse of this content and general copyright information, consult the [AMS Copyright Policy](https://www.ametsoc.org/PUBSReuseLicenses) (www.ametsoc.org/PUBSReuseLicenses).

However, the intermediate circulation still lacks accurate description due to the lack of comprehensive in situ observations and the numerical model drawbacks.

Strong western boundary currents (Fang et al. 2012; Wang et al. 2013; Quan et al. 2016) and mesoscale eddies (Wang et al. 2003; Xiu et al. 2010; Chen et al. 2011; Li et al. 2011; Lin et al. 2015; Zhang et al. 2016) could also be easily detected from the surface observations; that is, many mesoscale eddy activities are observed east of Vietnam. However, some mesoscale eddies appear in the subsurface and could not be observed on the surface (Song et al. 2019). Two anticyclonic eddies were detected in the subsurface of the southern SCS with in situ hydrography data (Zhang et al. 2014). Chen et al. (2015) found a mesoscale eddy in the deep layer of the northwestern SCS with mooring ADCPs. How the ocean circulation model captures the structure of the mesoscale eddy in the subsurface still needs to be researched.

An effective tool to improve our understanding of oceanography (i.e., intermediate circulation or mesoscale eddy) is data assimilation, which combines limited observations and numerical model. The previous ocean data assimilation in the SCS is mostly based on satellite data and in situ temperature and salinity (T/S) profiling data and mainly improves simulation of the temperature and salinity fields in the upper 1000 m. Data assimilation for the velocity field in the middle layer is usually neglected in the SCS due to a lack of velocity observations.

The international Argo program, which has been implemented since 2000, has enriched the number of observations in the middle layer to a certain extent (Wang et al. 2012a,b). Currently, the number of active floats in the global ocean is approximately 3900. Despite monitoring of the temperature and salinity in the upper ocean, the Argo float trajectory data also provide another way to study the current structure in the middle layer of the ocean (Park et al. 2004). Over last decade, a variety of methods have been explored for Lagrangian data assimilation (Kuznetsov et al. 2003; Molcard et al. 2003, 2005; Spiller et al. 2008; Muscarella et al. 2015; Slivinski et al. 2015). However, most of the studies are using simple model and synthetic observations, that is, from a model forecast. In fact, profile floats trajectories are influenced by vertical shear, surface drift and topography.

In the Mediterranean Forecasting System (MFS), the position information of the Argo trajectories has been directly assimilated with other observations [i.e., sea surface height (SSH), sea surface temperature (SST), and T/S profiles]. Retaining the state of the upper layer, simulation of the velocity structure at parking depth could be improved by 15% with Argo float trajectory data assimilation (Taillandier et al. 2006; Taillandier and

Griffa 2006; Nilsson et al. 2011, 2012). One big challenge on direct position assimilation is estimation of appropriate covariances, which is inherent nonlinearity (Castellari et al. 2001; Slivinski et al. 2015). Particle filter method can deal with the nonlinearity (Slivinski et al. 2015), but it is rarely used in ocean data assimilation. Instead of assimilating the original trajectory directly, we estimate the middepth (~ 1200 m) velocity field from the Argo float trajectory and then assimilate the estimated velocity observation into the model to circumvent this problem. Since the velocity is already included in the ocean model, the usage of middepth velocity observations allows us to forgo additional trajectory prediction models, which is a difficult task. In addition, the assimilation of Argo trajectories has not yet been used in the SCS, which is another focus of this study.

The study is organized as follows: In section 2, the middepth velocity estimation method from Argo trajectories and corresponding quality control are introduced. In section 3, the experimental setup of ocean data assimilation for the estimated velocity at the parking depth is described. In section 4, the simulation results are analyzed. Finally, conclusions and suggested corresponding future work are presented in section 5.

2. Velocity retrieval and 4DVAR

The proposed Argo trajectory assimilation method is composed of the estimation and assimilation of middepth velocity. In this method, the quality control and observation error estimation of the velocity data are two important aspects. The assimilation technique uses four-dimensional variational data assimilation (4DVAR). The background error covariance in 4DVAR is implicitly developed with the ocean state during the assimilation time window; thus, 4DVAR is more suitable than 3DVAR for data assimilation of sparse velocity observations.

a. Middepth velocity retrieval

Several methods have been provided to estimate the velocities at parking depth (Park et al. 2005; Xie and Zhu 2008; Lebedev et al. 2007; Ollitrault and Rannou 2013), which were then applied to estimate the regional or global ocean circulation at the basin scale (Voet et al. 2010; Park and Kim 2013; Ollitrault and Colin de Verdière 2014; Markova and Bagaev 2016; Wang et al. 2018). In this paper, the method provided by Park et al. (2005) is adopted due to the method's high level of accuracy.

The estimation of middepth velocity \mathbf{v}_{deep} is based on

$$\mathbf{v}_{\text{deep}} = \Delta \mathbf{r} / \Delta t, \quad (1)$$

where $\Delta \mathbf{r}$ and Δt is the drift distance and time within the subsurface. The difference between different methods is how the float trajectory is treated on the surface, that is, how the descend start point P_{DS}^n and ascend end point P_{AE}^n is treated. In Park's method, one advantage is taking the linear velocity and the inertial velocity into consideration during the accurate estimation of P_{DS}^n and P_{AE}^n . The other advantage is that instead of using linear extra interpolation, an extra interpolation method based on a least squares fit of trajectory positions is adopted to estimate P_{DS}^n and P_{AE}^n and surface velocity. According to Park et al. (2005), the subsurface velocity \mathbf{v}_{deep}^n at the parking depth can be written as follows:

$$\mathbf{v}_{deep}^n = \frac{P_{AE}^{*n} - P_{DS}^{*n}}{\Delta t} + E_{AE}^n - E_{DS}^n - E_T^n, \quad (2)$$

where P_{DS}^{*n} and P_{AE}^{*n} are the estimation of P_{DS}^n and P_{AE}^n , E_{AE}^n and E_{DS}^n are the errors due to the inaccuracy of P_{DS}^n and P_{AE}^n , respectively, and E_T^n is the error related to velocity shear. Although the Argo trajectories include the tidal current information, according to the previous studies, the error introduced by tides are much smaller than the error introduced by the inaccuracy of satellite surface positioning and vertical velocity shear (Park et al. 2004; Lebedev et al. 2007; Ollitrault and Rannou 2013). Thus, the time-averaged middepth velocity from Argo trajectories in this study are treated as not include tides. Park et al. (2005) estimated the total error ($E_{AE}^n - E_{DS}^n - E_T^n$), about 0.2 cm s^{-1} with over six satellite position points at surface, which confirms the accuracy of the estimated velocity.

b. Quality control procedure for velocity

Before assimilation into the model, two rounds of quality control are employed for higher velocity accuracy. The first round of quality control is applied to the original trajectories of the Argo float before velocity estimation, which is completed in four steps (Wang et al. 2018). The first step is removing the points if the distance between two adjacent points is larger than 1.5° ; the second step is eliminating data if the time does not satisfied $T_N^{n-1} < T_{DS}^n < T_{AE}^n < T_1^n$ (T_N^{n-1} is the last satellite positioning point in the $(n-1)$ th cycle and T_1^n is the first satellite positioning point in the n th cycle); in the third step, data are discarded if the satellite observational position is less than one in the n th cycle; and in the fourth step, the time information of the nearest satellite position is used if T_{DS}^n or T_{AE}^n is missing.

The second round of quality control is applied to the velocity at parking depth, which is finished in two steps. The first step is discarding data with a speed of less

than 1 cm s^{-1} (account for 10.1% of the total), which is comparable to the total error defined in section 2a (approximately 0.2 cm s^{-1}) (Park et al. 2005). The second step is discarding velocity if the parking depth changed dramatically during the adjacent cycles (account for 7% of the total), for example, the parking depth jumped from 1200 m to several hundred meters suddenly, and jumped back to 1200 m.

After quality control, the middepth velocities have been used to estimate the current structure of the basin scale in the SCS (Wang et al. 2018), indicating a cyclonic circulation at 1200 m in northern SCS. The root-mean-square error (RMSE) of middepth velocities with YoMaHa'07 (Lebedev et al. 2007) product is 1.28 cm s^{-1} for zonal and 1.11 cm s^{-1} for meridional (Wang et al. 2018).

It should be mentioned that the middepth velocity obtained in section 2a is time-averaged velocity during the drifting period in the subsurface instead of the instantaneous velocity. Correspondingly, the background field should also use the time-averaged velocity field during the same parking period, which is difficult to satisfy due to the variation in the drifting period for different Argo floats. As an alternative choice, the middle time and position during the drifting period is considered to be the observation time and position in this study.

3. Experimental setup for trajectory-derived velocity assimilation

The western SCS is characterized by a dominant western boundary current (SCSWBC) and an active mesoscale process. The mean speed is approximately $12\text{--}16 \text{ cm s}^{-1}$ at 1000 m in the western SCS (Zhou et al. 2010). When an Argo float moved to the western SCS, the Argo float more easily captured by the dominant processes. Thus, the western SCS is selected as the area in which to study the impact of the Argo trajectory data assimilation on the middepth current structure. During the study period, float 5903457 had just moved into the western SCS and therefore it was studied with an intense focus.

a. Estimation of model states

The assimilations system is SCS 4DVAR system, which combined the Regional Ocean Modeling System (ROMS; version 3.7; <https://www.myroms.org>) and observations using the primal formulation of incremental strong constraint 4DVAR (IS4DVAR) (Moore et al. 2011a,b). In ROMS-IS4DVAR method, the best estimation of ocean states can be obtained by minimizing the cost function:

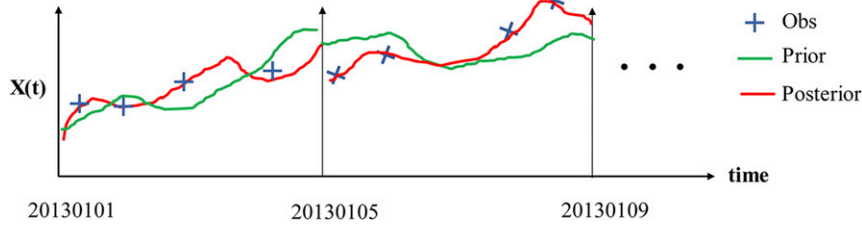


FIG. 1. The process of continuous data assimilation in 4DVAR; $X(t)$ denotes the model states at time t .

$$J(\delta \mathbf{x}, \delta \mathbf{f}, \delta \mathbf{b}) = \frac{1}{2} \delta \mathbf{x}^T \mathbf{B}_x^{-1} \delta \mathbf{x} + \frac{1}{2} (\mathbf{H} \delta \mathbf{x} - \mathbf{d})^T \mathbf{R}^{-1} (\mathbf{H} \delta \mathbf{x} - \mathbf{d}) + \frac{1}{2} \delta \mathbf{f}^T \mathbf{B}_f^{-1} \delta \mathbf{f} + \frac{1}{2} \delta \mathbf{b}^T \mathbf{B}_b^{-1} \delta \mathbf{b}, \quad (3)$$

where \mathbf{x} denotes the state vector (T, S, ζ, u, v), \mathbf{f} denotes the atmosphere forcing (wind stress, heat flux), and \mathbf{b} denotes the lateral open boundary conditions. Other terms in (3) are as follows: $\mathbf{d} = \mathbf{y} - H(\mathbf{x})$ is the innovation vector that represents the difference between observations and model analog in observation space, and \mathbf{B}_x , \mathbf{B}_f , \mathbf{B}_b , and \mathbf{R} are the error covariance matrices for background field, surface forcing, lateral boundary conditions, and observations.

In ROMS-IS4DVAR, the increments of model states are separated into balanced and unbalanced components. All the balance components are based on the T increments δT , which is estimated by minimizing the cost function (3) (Weaver et al. 2005). The balanced S field is estimated through nonlinear T - S relationship; the balanced density field is estimated through nonlinear equation of state of δT and δS ; SSH is diagnosed as a function of $\delta \rho$ (baroclinic part) and $(\delta u, \delta v)$ (barotropic part); the balanced pressure increment δp is computed by hydrostatic equation; finally, the dynamically consistent velocity field is obtained through geostrophic balance except near the equator. Thus, a dynamically consistent mass field is obtained first, then a dynamically consistent velocity field. The mid-depth velocity assimilation influenced the model velocity field through the unbalanced components, which propagated horizontally and vertically through correlation matrix (expressed as the solution of a diffusion equation), then influenced other variables through model dynamics.

The assimilation procedure is shown in Fig. 1. Observations are continuously assimilated into the model in all assimilation experiments every 4 days (equal to the working cycle of Argo floats in SCS). Specifically, in one cycle, for example, the model integrates from 1 to 5 January 2013 (denoted as “Prior”;

Fig. 1, green line) to provide background fields and extract model value in observation space. Then the model states are adjusted through 4DVAR. After assimilation, the model initialized from the analysis field at 1 January 2013 and integrated to 5 January 2013 again (denoted as “Posterior”; Fig. 1, red line). In next cycle, the model starts from the end states of previous cycle (1–5 January) and repeat the progress until the end date (28 February 2013). All experiments were conducted for 2 months, with a total of 15 data assimilation cycles.

b. Model configuration

The generic length scale (GLS; Warner et al. 2005), k - ω vertical mixing scheme, harmonic horizontal viscosity (mixing coefficient: $4 \text{ m}^2 \text{ s}^{-1}$), no slip boundary conditions, quadratic bottom friction (bottom drag coefficient: 2.5×10^{-3}) and sponge layer are employed as the SCS ROMS configuration. The model domain covers part of the northwestern Pacific Ocean (1° – 30°N , 99° – 134°E) with a horizontal resolution of $1/10^\circ$ and 24 vertical levels. The bathymetry is derived from GEBCO08 with a minimum depth of 10 m and a maximum depth of 5500 m (Fig. 2).

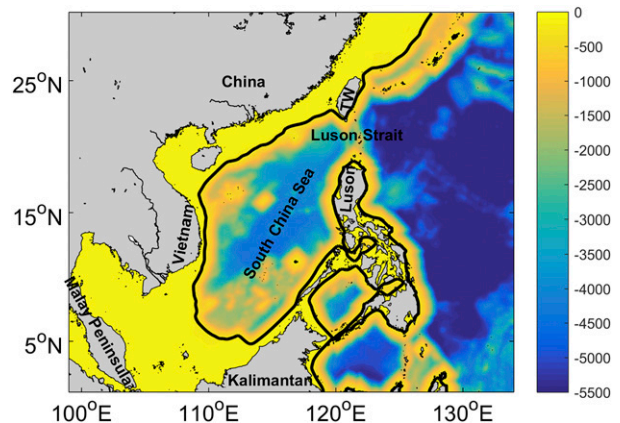


FIG. 2. Bathymetry (m) and model domain (1° – 30°N , 99° – 134°E). The black contour represents the 200-m isobath. TW represents Taiwan Island.

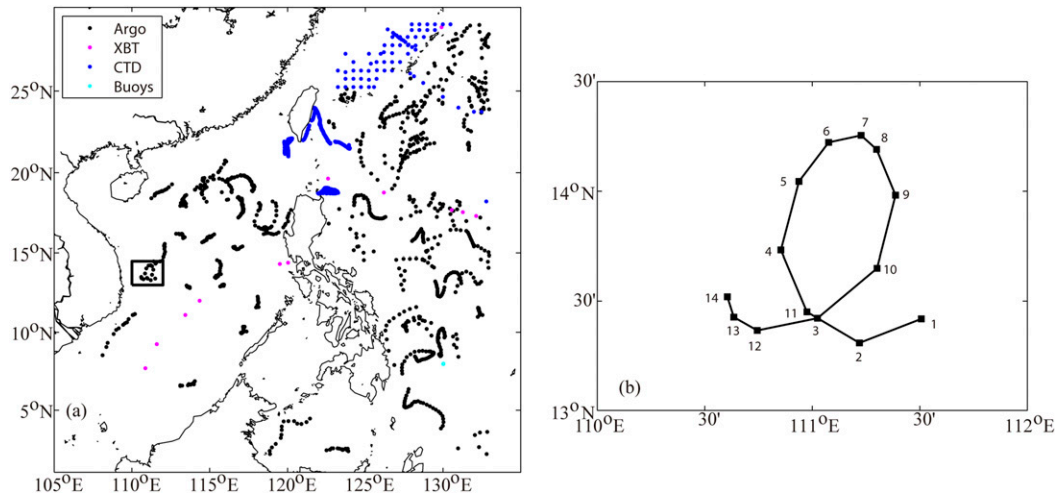


FIG. 3. Distribution of (a) in situ observations and (b) Argo float 5903457 T/S profile positions during 1 Jan–28 Feb 2013. The range in (b) is marked by a black box in (a); the numbers in (b) represent the observational sequence in the first 2 months of 2013.

The model is initialized from climatological Simple Ocean Data Assimilation (SODA) data and is forced by a climatological forcing (COADS) for 10 years, which is considered to be the model spinup process. Then, the model is integrated for the period of 2000–15, which is forced by real surface forcing and boundary conditions. The heat and freshwater fluxes are extracted from the ECMWF interim reanalysis (ERA-Interim) dataset (<https://apps.ecmwf.int/datasets/data/interim-full-daily>) with a horizontal resolution of 0.75° and a temporal resolution of 6 h (Dee et al. 2011). The wind stresses are calculated using the bulk formula with 10-m U -wind and V -wind components from the cross-calibrated multiplatform (CCMP), version 2.0 (Atlas et al. 2011; <ftp://ftp2.remss.com>), with a horizontal resolution of 0.25° and a temporal resolution of 6 h. The southern, eastern, and northern boundaries adopt open boundary conditions from SODA, version 3.3.1 (Carton et al. 2018; <https://www.atmos.umd.edu/~ocean/>), while the west boundary is closed. In detail, radiation and nudging boundary conditions are chosen for the 3D variables (i.e., u , v , temperature and salinity), Flather boundary conditions are chosen for the depth-integrated velocity components, and clamped boundary conditions are chosen for the free surface.

Tides are not included in our model. It is challenging for assimilating altimetry data into a model include tide, since tides are high frequency signal compared to the mesoscale variability. Xie et al. (2011) compared the model fields with or without tides, the differences are minor on monthly averaged velocity field and the influence on temperature and salinity decreased with depths below 100 m. The T/S difference between with or

without tide are about 0.2°C (0.05 psu) $^{-1}$ (Wang et al. 2017). For simplicity, tides are excluded in the model in this study.

c. Observations

The observations used in the data assimilation experiments are satellite altimeter data (SSH), satellite SST, in situ T/S profiling data and Argo trajectory-derived middepth velocity data. The SSH data are delayed time, and gridded maps of sea level anomaly (MSLA) data from AVISO (before 2016, <http://www.aviso.oceanobs.com/duacs/>). The blended SST

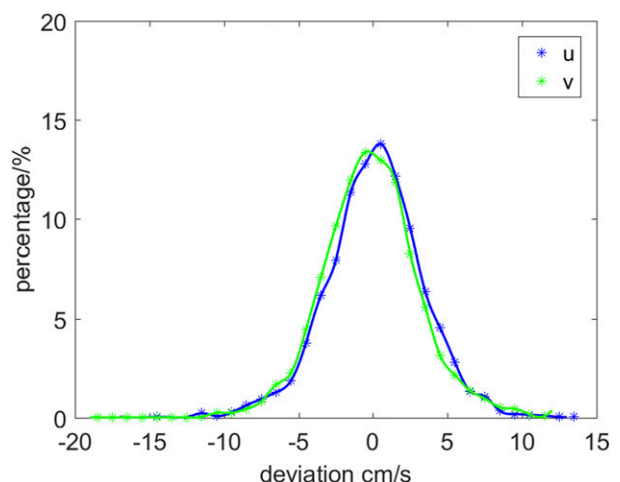


FIG. 4. Distribution of velocity deviation between HYCOM-NCODA product and Argo data at 1200 m during 2006–16. Blue is the distribution of zonal ocean current u , and green is the distribution of meridional ocean current v .

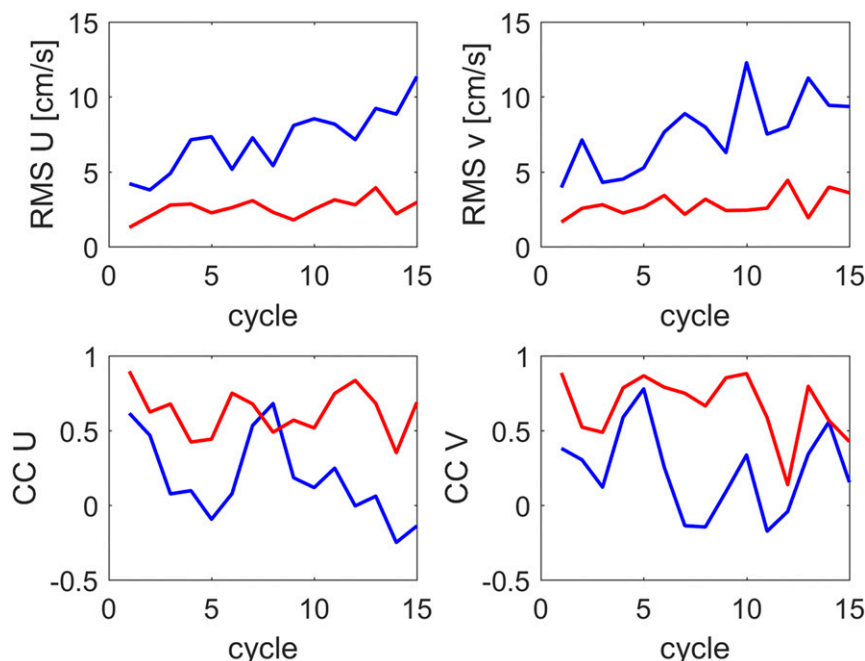


FIG. 5. (top) RMSEs and (bottom) CCs of (left) u and (right) v for different observation error standard deviations in January and February 2013. The red line represents the result of experiment with an observation error of 2 cm s^{-1} , and the blue line represents the result of experiment with an observation error of 5 cm s^{-1} .

data used in the experiments are version 2 AVHRR-only products produced by NOAA (Reynolds et al. 2007; [ftp://eclipse.ncdc.noaa.gov](http://eclipse.ncdc.noaa.gov)). Both SSH and SST data are available every day with a horizontal spatial resolution of 0.25° . The in situ data (Argo, CTD and XBT, etc.) are the quality-controlled temperature and salinity profiles from the ENSEMBLES project (EN4.2.1) provided by the Met Office Hadley Center (Good et al. 2013; <http://hadobs.metoffice.com/en4/download.html>, Fig. 3a). Before assimilated into the model, the T/S profiles were interpolated to 23 z levels: $-5, -10, -15, -20, -25, -30, -35, -40, -50, -60, -75, -100, -125, -150, -200, -250, -300, -400, -500, -600, -800, -1000$, and -1200 m . This interpolated data may cause redundancy somewhere due to the ROMS terrain-following coordinate system. However, some error data in a single profile will be eliminated simultaneously. The Argo trajectory data were provided by the Coriolis Operational Oceanography data center ([ftp://ftp.ifremer.fr/ifremer/argo](http://ftp.ifremer.fr/ifremer/argo)).

The observation errors are assumed to be uncorrelated at any time or at any point as defined in most ocean data assimilation systems. The variances along the main diagonal of observation error covariance are a combination of measurement error and representative error. Measurement errors from different data sources are obtained with the following standard deviations

(Moore et al. 2011b): 2 cm for SSH, 0.4°C for SST, 0.1°C for in situ temperature T , and 0.01 psu for in situ salinity S .

For the middepth velocity, since the Argo positions are not perfect, a total error is given without distinguishing different error sources that are mentioned in section 2a. This total error is estimated through the Hybrid Coordinate Ocean Model–Navy Coupled Ocean Data Assimilation (HYCOM-NCODA; http://tds.hycom.org/thredds/dodsC/GLBu0.08/exp_90.9) product (as shown in Fig. 4). Most of the misfits are distributed between -5 and $+5 \text{ cm s}^{-1}$ (accounting for approximately 83% of the total number), and the standard deviation of these misfits (between -5 and $+5 \text{ cm s}^{-1}$) is about 2 cm s^{-1} . Thus, the observation error has been tested with standard deviations of 2 and 5 cm s^{-1} for the 2-month assimilation.

TABLE 1. Experimental design. The assimilated observations are marked with Y; otherwise, the observations are marked with N. The columns show SST (satellite SST), SLA (sea level anomaly observation), T (in situ temperature profile), S (in situ salinity profile), and VEC (velocity derived from Argo trajectory).

Expt name	SST	SLA	T/S	VEC
Ctrl	N	N	N	N
Exp1	Y	Y	N	N
Exp2	Y	Y	Y	N
Exp3	Y	Y	Y	Y

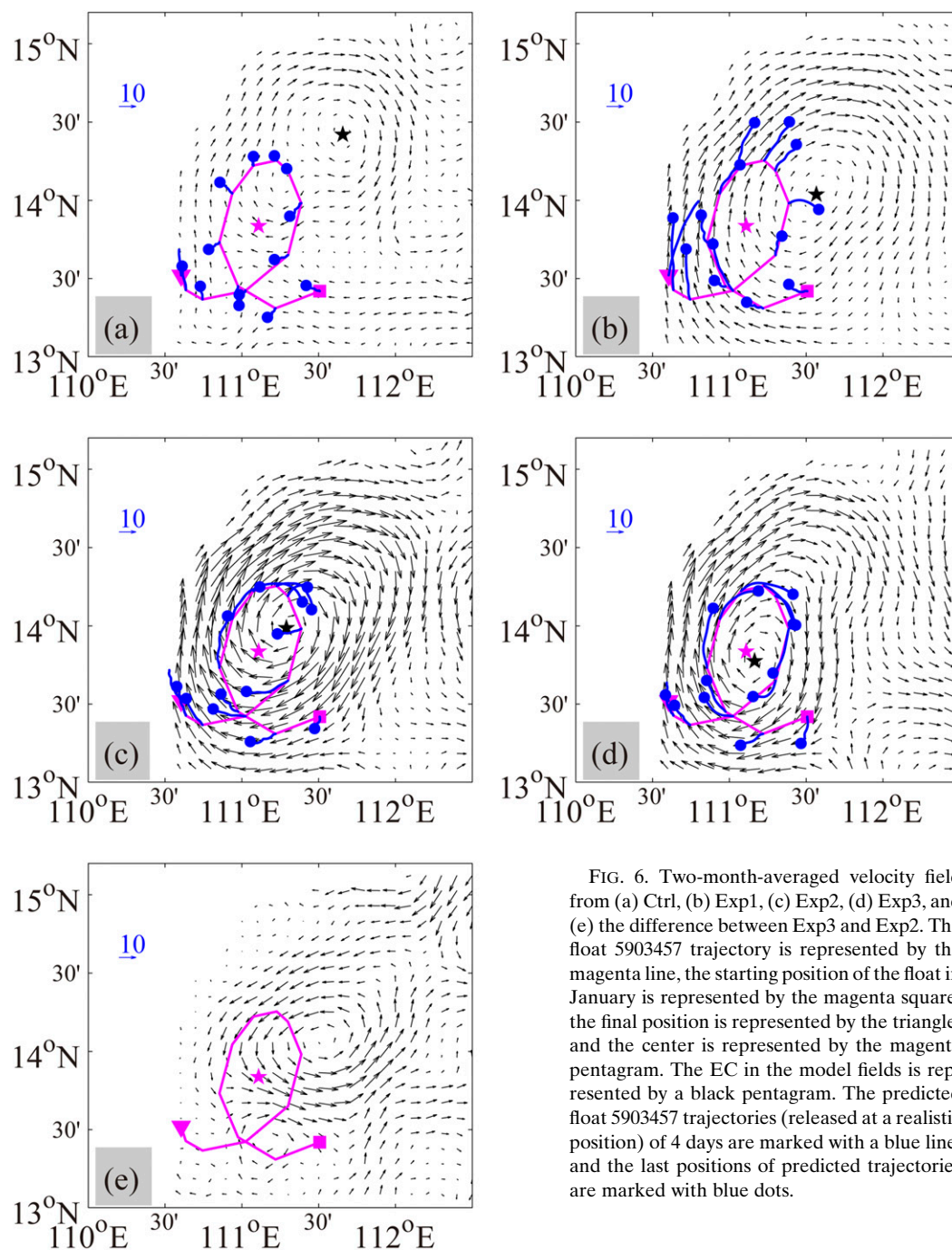


FIG. 6. Two-month-averaged velocity field from (a) Ctrl, (b) Exp1, (c) Exp2, (d) Exp3, and (e) the difference between Exp3 and Exp2. The float 5903457 trajectory is represented by the magenta line, the starting position of the float in January is represented by the magenta square, the final position is represented by the magenta triangle, and the center is represented by the magenta pentagram. The EC in the model fields is represented by a black pentagram. The predicted float 5903457 trajectories (released at a realistic position) of 4 days are marked with a blue line, and the last positions of predicted trajectories are marked with blue dots.

The total RMSEs and correlation coefficients (CCs) of the middepth (u , v) with Argo trajectory-derived (u , v) are shown in Fig. 5 (since there are no direct velocity observations, the Argo trajectory-derived velocities are used as the true velocities). As the 2 cm s^{-1} velocity error performed better than the 5 cm s^{-1} velocity error, with smaller RMSEs (2.6 cm s^{-1} for u and 2.8 cm s^{-1} for v) and higher CCs (0.66 for u and 0.69 for v). The

observation error of the middepth is set to 2 cm s^{-1} in this study.

d. Experimental design

Four experiments were designed to evaluate the Lagrangian velocity assimilation influence on the model forecast (Table 1). The reference experiment does not assimilate any data (Ctrl). In Exp1, only satellite data

TABLE 2. RMS misfits between model values and observations at 1200 m for EC, u , v , and position misfit. The CCs placements are in parentheses. The eddy center from the model output (EC) is the location of the minimum speed in the eddy. The EC (13.8°N, 111.1°E) of the trajectory observations is identified by eight nearly symmetrical points (3, 4, 5, 6, 8, 9, 10, and 11 in Fig. 3b) of the trajectory, i.e., the position where the sum of the distance to these points is the shortest.

	Ctrl	Exp1	Exp2	Exp3
EC (km)	87.7	54.1	25.6	0.9
U (cm s ⁻¹)	6.1 (-0.15)	6.1 (0.22)	3.9 (0.81)	3.2 (0.87)
V (cm s ⁻¹)	7.2 (0.06)	10.9 (-0.51)	7.7 (0.58)	2.5 (0.94)
Distance (km)	25.5	31.2	18.2	16.4

(SST and SLA) are assimilated. In Exp2 both satellite data and in situ T/S profile data are assimilated. In Exp3, additional Argo trajectory-derived middepth velocities are added to the Exp2 dataset. In Exp1 to Exp3, the

assimilation window is 4 days. All experiments begin from the same initial conditions (model's the real forecast on 1 January 2013) and are driven by the same surface forcing and boundary conditions. To evaluate the effects of assimilating different data more accurately, the climatological nudging has been closed in all assimilation experiments.

4. Results analysis

During the first 2 months in 2013, there were 88 active Argo floats in the whole model region, among which 23 Argo floats were distributed in SCS. After quality control, these floats provided 382 middepth velocity observations in January and February 2013 (Fig. 3a). The mean parking depth is 1179 m, and 358 observations deeper than 1100 m (accounting for ~94% of the total

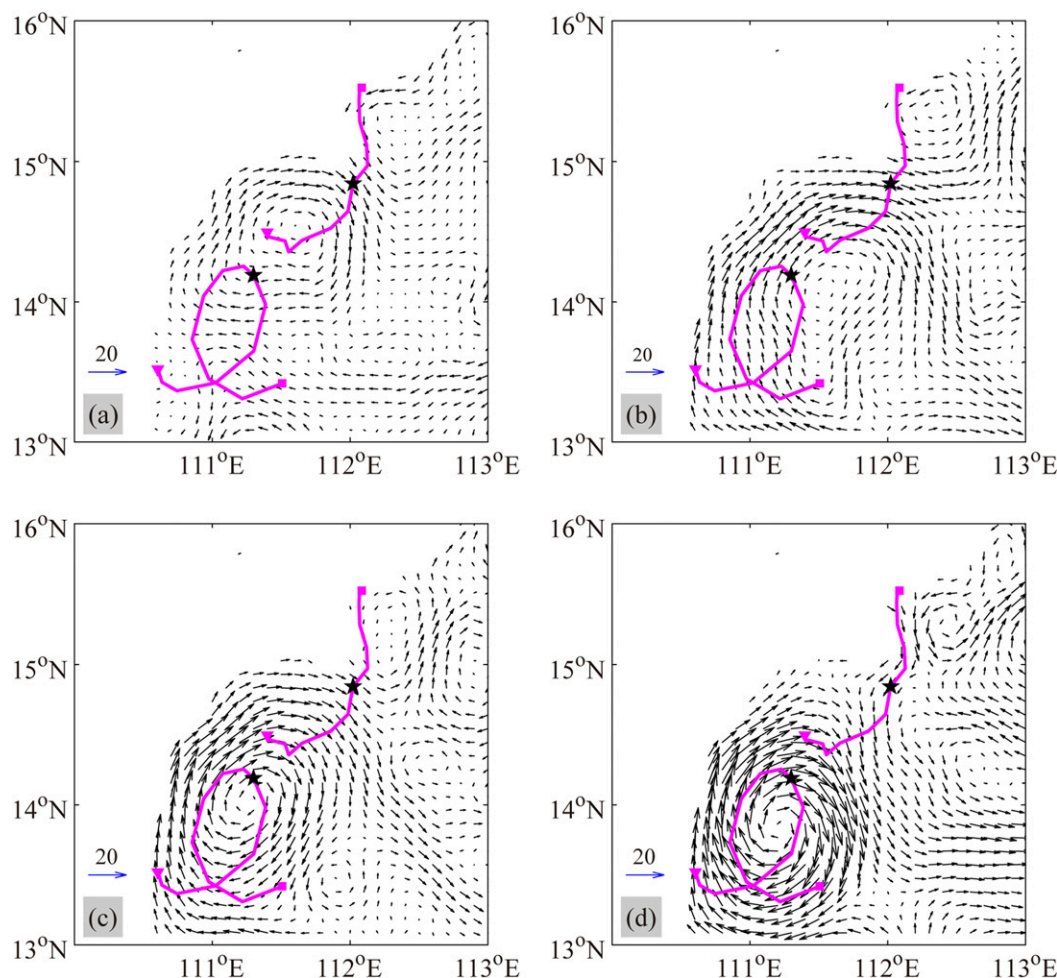


FIG. 7. Month-averaged velocity field at 1200 m in January 2013 for (a) Ctrl, (b) Exp1, (c) Exp2, and (d) Exp3. The float 5903457 and 5902163 trajectories are represented by the magenta lines, the starting positions of the floats in January are represented by the squares, and the final positions are represented by the triangles. The pentagrams denote the locations of the floats on 31 Jan 2013.

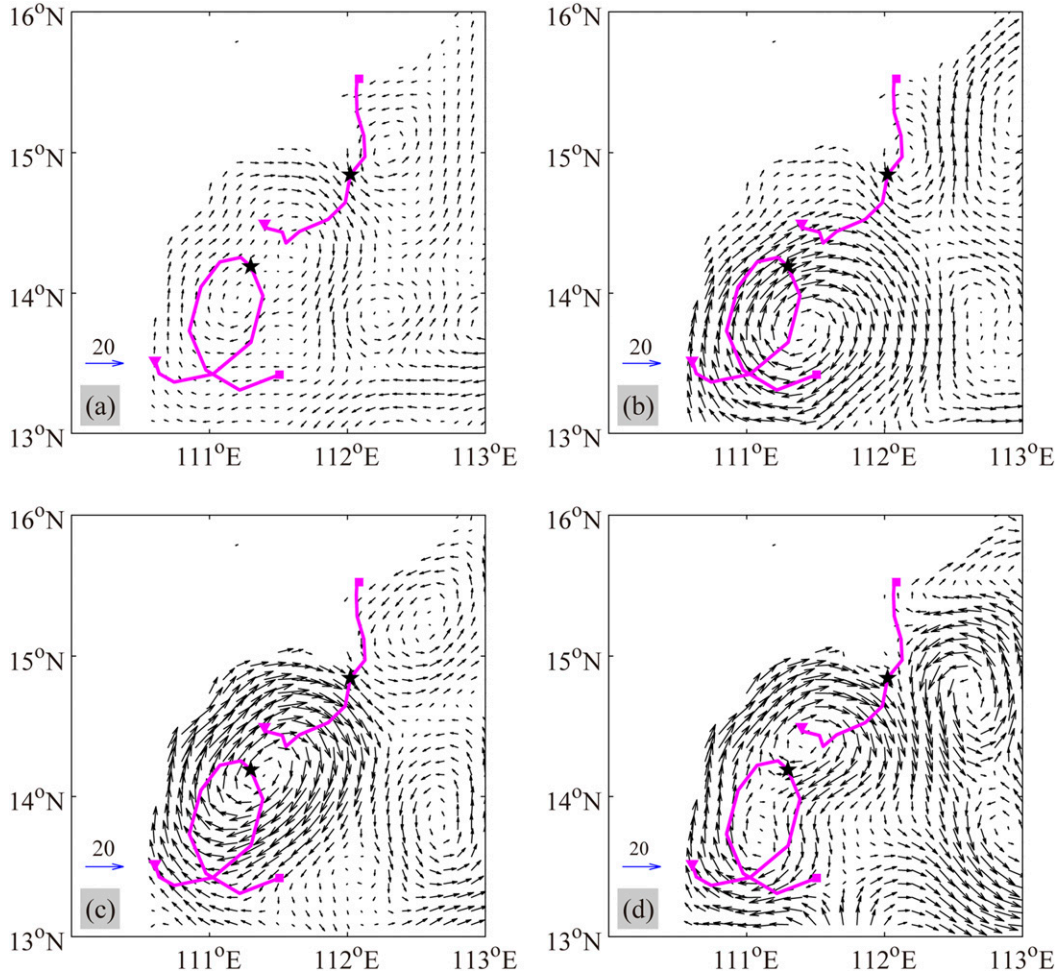


FIG. 8. Month-averaged velocity field at 1200 m in February 2013 for (a) Ctrl, (b) Exp1, (c) Exp2, and (d) Exp3. The float 5903457 and 5902163 trajectories are represented by the magenta lines, the starting positions of the floats in January are represented by the squares, and the final positions are represented by the triangles. The pentagrams denote the locations of floats on 31 Jan 2013.

number). The mean speed is 3.4 cm s^{-1} with a maximum speed of 13.1 cm s^{-1} . The Argo floats were mainly irregularly distributed in the northern SCS (Fig. 3a). Two floats are in western SCS: float 5903457 completed a cycle near the east coast of Vietnam in January–February 2013 and float 5902163 drifted southwestward. The following analysis is mainly based on the float 5903457 float (Fig. 3b) and with less focus on float 5902163.

a. The impacts of different assimilation experiments in the western SCS

The impacts of assimilating different observations were compared based on the 2-month-averaged current structure at 1200-m depth, as shown in Fig. 6. An anticyclonic eddy appeared at $\sim 14^\circ\text{N}$ in all experiments, while apparent differences are identified, such as eddy radius, position of eddy center (EC) and speed.

These observation influences on middepth velocity field can be expressed as

$$\delta \mathbf{v}^k = K_{vT} \delta T^k + K_{vS} \delta S^k + K_{v\zeta} \delta \zeta^k + \delta \mathbf{v}_U^k, \quad (4)$$

where K_{vT} , K_{vS} , and $K_{v\zeta}$ are balance operator based on geostrophic balance, δT^k , δS^k , and $\delta \zeta^k$ are balanced increments of T , S , and SSH, and $\delta \mathbf{v}_U^k$ is the unbalanced increment of velocities u and v .

In Exp1, the assimilation of SLA and SST introduced barotropic and baroclinic adjustment into velocity field, among which the barotropic adjustment is dominant, and yielded the largest radius of an eddy in Exp1 (Fig. 6b) at approximately 104 km (defined as the distance of model EC to the western boundary). The barotropic and baroclinic geostrophic adjustment together narrowed the radius of the eddy to 74 km in Exp2 (Fig. 6c). However,

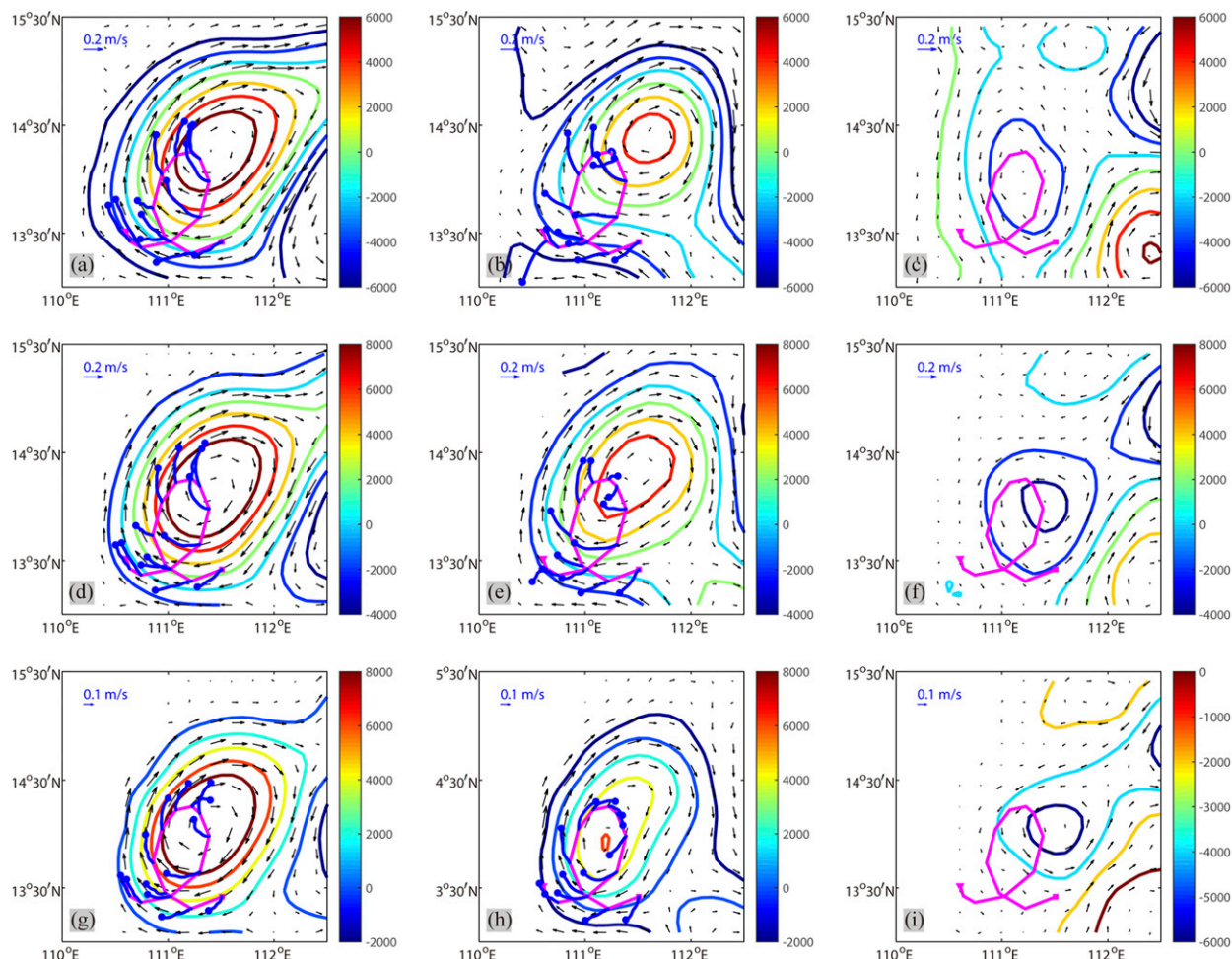


FIG. 9. Two-month-averaged velocity field of (left) Exp2, (center) Exp3, and (right) the difference between them (Exp3 – Exp2). Depths are (top) 500, (middle) 750, and (bottom) 1000 m. Contours represent streamfunction (interval: $2000 \text{ m}^2 \text{ s}^{-1}$). The float 5903457 trajectory is represented by the magenta line. The predicted float 5903457 trajectories (released at a realistic position) of 4 days are marked with blue lines, and the last positions of predicted trajectories are marked with blue dots.

the increments introduced by the balance operator (i.e., $K_{VT}\delta T^k + K_{VS}\delta S^k + K_{VZ}\delta \zeta^k$) are part of the geostrophic currents (i.e., $\delta \mathbf{v}^k$). In Exp3, the radius further decreased to 61 km due to the introduction of middepth velocities (Fig. 6d). Except the balanced components through geostrophic adjustment, the unbalanced components (i.e., $\delta \mathbf{v}_U^k$) are also adjusted in Exp3.

Along with the changes in radius, the position of the EC changed. The EC of Exp3 is obviously closest to the EC of the float 5903457 trajectory. The EC in Exp2 is closer than in Exp1, proving that assimilation of in situ T/S profile observations is necessary for improving subsurface states. The EC misfits between the model and trajectories are listed in Table 2. The misfit between Exp3 and the observations is the smallest (approximately 0.9 km), followed by Exp2 (approximately 25.6 km). When the balanced components in the velocity increment are

overly strong, an opposite correction is made through the introduction of unbalanced components in the velocity increment (Fig. 6e).

The impact on trajectory prediction had also been compared in Fig. 6. Due to the topography, the particles mainly went northward in January 2013, which could be seen in all assimilation experiments. However, obvious differences occurred in February 2013. The particles released in Exp3 moved almost along the realistic trajectories, while in Exp1 and Exp2 the particles drifted away from realistic trajectories. The movements of particles, approximately two-dimensional in 4 days, were in agreement with the Eulerian velocity field. Thus, an improvement of Lagrangian velocities could be expected with the improvement of Eulerian velocity field. This improvement was quantified in terms of relative differences (%) between Exp3 and Exp2 float position

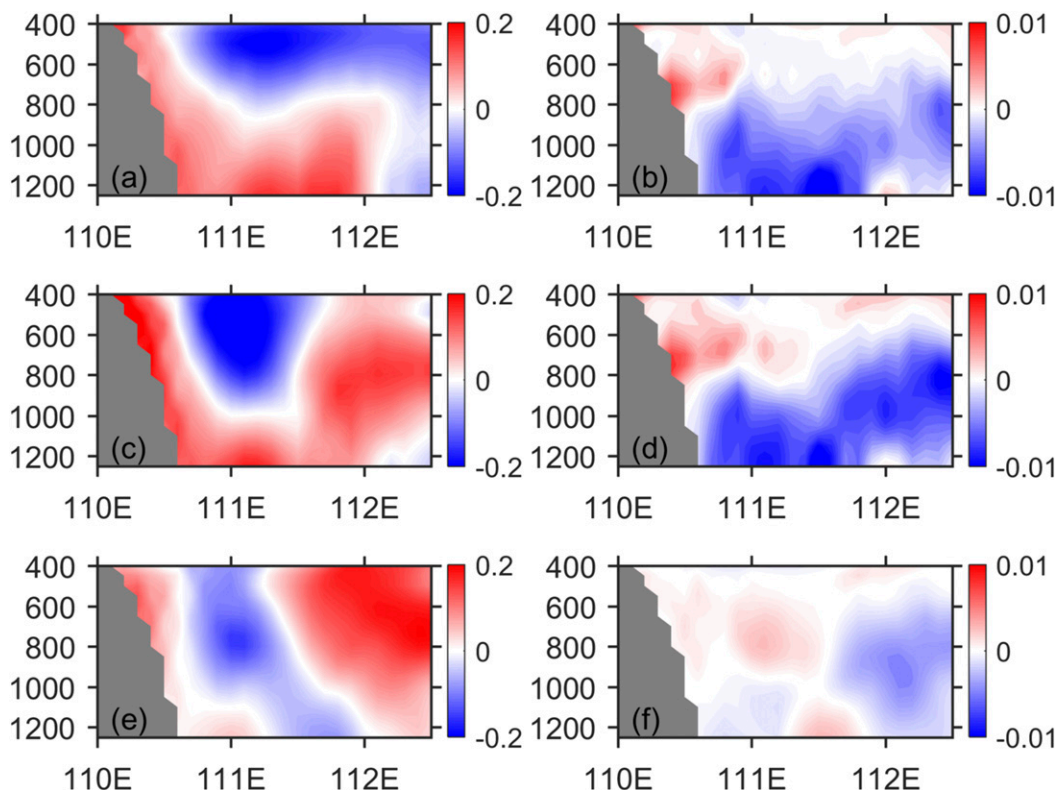


FIG. 10. (a),(c),(e) Temperature and (b),(d),(f) salinity zonal transects (along 13.8°N) of the differences (top) between Exp2 and Ctrl, (middle) between Exp3 and Ctrl, and (bottom) between Exp3 and Exp2.

misfits (16.4 and 18.2 km, respectively, in Table 2) and found to be about 7% (take the Ctrl as a reference).

Except for float 5903457, float 5902163 is also in the western SCS. All experiments showed that float 5902163 affected by a cyclonic eddy and move southward in January 2013 (Fig. 7). However, the velocity field in Exp3 was closer to the float 5902163 trajectory after the float left land boundary at the end of January (23–31 January 2013) with introducing of middepth velocities. In February, the velocity field was affected by both floats (floats 5903457 and 5902163; Fig. 8). As a result, the core of the anticyclonic eddy in Exp3 was distorted and closer to the north land boundary than in Exp2. Thus, this float can be captured by the south edge of eddy core in Exp3 and go westward.

b. Vertical propagation of corrections

The velocity corrections at ~1200 m are likely to propagate vertically due to the cross-correlation in the background error covariance, and propagate forward through the model dynamics. This vertical propagation has been studied above the parking depth of the float 5903457 (Fig. 9). In Exp2, the eddy structure at different depths is similar, such as the radius and position of EC. The EC distance between 500 and 1000 m is only

20.9 km, which means that the eddy is almost vertically distributed without tilt. When the middepth velocities are assimilated, the radius (especially in the zonal direction) of the eddy decreases with depth, and the EC moves southwest, approaching the trajectory structure. The EC distance between 500 and 1000 m increases to 75.5 km in Exp3, which means the EC tilts toward the southwest.

The vertical influence could also be seen from predicted trajectories at different depth. The predicted trajectories in Exp2 and Exp3 were consistent with Eulerian velocity field at different depth, as at parking depth. In Exp3, the position misfits amplified with the increase of distance to parking depth, indicating that the influence of middepth velocity was weakened with the increase of distance. (This could also be proved from Figs. 11 and 12, in which the difference between Exp2 and Exp3 are little at surface.) This probably one reason for the EC tilt with depth.

The assimilation of the middepth velocity also yielded changes in the mass field through model dynamics, that is, advection process. A zonal transect through trajectory EC (13.8°N, 111.1°E) is shown in Fig. 10. In Exp2, a cold core is distributed mainly between 110.5° and 112°E, which is broader than the diameter of the trajectory

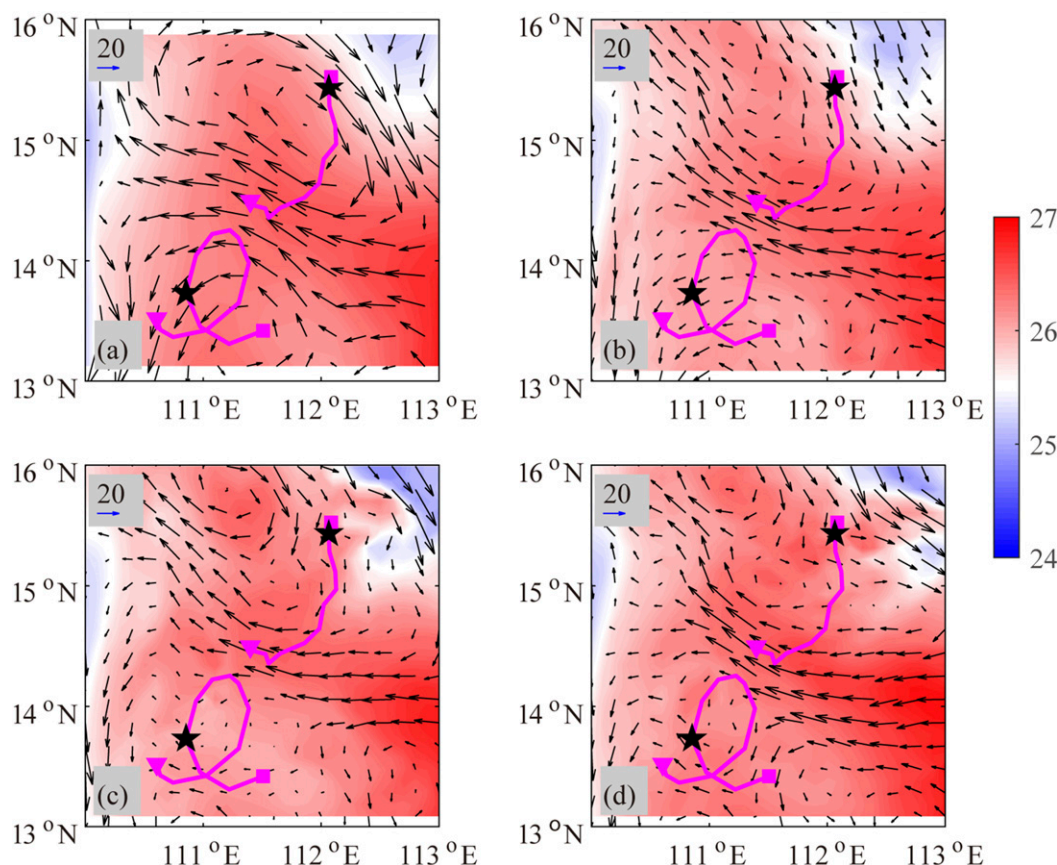


FIG. 11. The SST on 15 Jan 2013 for (a) AVHRR, (b) Exp1, (c) Exp2, and (d) Exp3. The vectors are surface geostrophic currents. The surface geostrophic currents in (a) are from AVISO, and the others are from model results. The float 5903457 and 5902163 trajectories are represented by the magenta lines, the starting positions of the floats in January are represented by the squares, the final positions are represented by the triangle, and the pentagrams denote the locations of floats on 15 Jan 2013.

(Fig. 6). In Exp3, the cold-core diameter is narrowed (between 110.5° and 111.5°E) and more consistent with the float trajectory. The largest change in the temperature fields ($\sim 0.2^{\circ}\text{C}$) due to velocity correction is approximately 600–1000 m (Fig. 10e), although the float parking depth is approximately 1200 m. The contribution of velocity corrections to the salinity field is on the order of 0.005 psu (Fig. 10f).

Although Argo floats are important for the subsurface states, SST and SLA are more important at surface. The assimilation of Argo T/S profile and middepth introduced some errors in the velocity field at the region near floats (Figs. 11 and 12), but the main pattern is similar to Exp2 and observations. It should be mentioned that the movement of float 5903457 was in contrast to the surface velocity (Fig. 11a) field, indicating that the eddy in 1200 m cannot be detected from surface. Differing from float 5903457 was the trajectory of float 5903163 drifting from northeast to southeast at surface (Fig. 11) and 1200 m (Fig. 7). An anticyclonic eddy appeared near

float 5902163 in January and disappeared in February at surface (Figs. 11a and 12a). All assimilation experiments captured the pattern at surface due to the assimilation of satellite data. However, influenced by the topography, the anticyclonic eddy near float 5902163 cannot extend to 1200 m (Figs. 7 and 8). The slow movement ($\sim 3 \text{ cm s}^{-1}$) of float indicated that this float was also influenced by the middepth velocity field.

c. System compatibility

When adding a new dataset, it is important that the forecast quality of the SST, SLA, T profile, and S profile not decrease. The compatibility of the trajectory with other observations in the 4DVAR system was checked through statistical analysis. The RMSEs between the model field and observations are defined as follows:

$$\text{RMSE}(x) = \sqrt{\sum_{i=1}^N (x_i^{\text{model}} - x_i^{\text{observation}})^2 / N}, \quad (5)$$

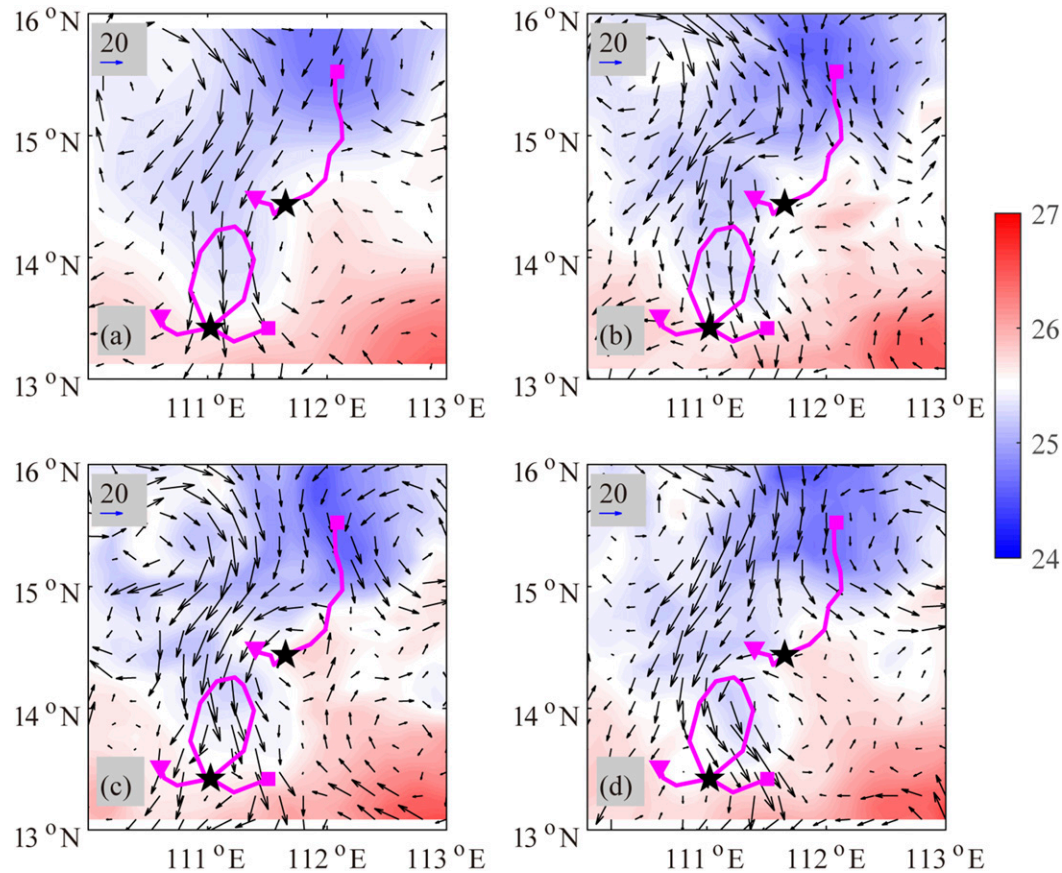


FIG. 12. The SST on 14 Feb 2013 for (a) AVHRR, (b) Exp1, (c) Exp2, and (d) Exp3. The vectors are surface geostrophic currents. The surface geostrophic currents in (a) are from AVISO, and the others are from model results. The float 5903457 and 5902163 trajectories are represented by the magenta lines, the starting positions of the floats in January are represented by the squares, the final positions are represented by the triangles, and the pentagrams denote the locations of floats on 14 Feb 2013.

where x denotes the SST, SLA, T (temperature profile), or S (salinity profile), and N is the total number of term x for 2 months. In terms of SST and SLA, only water depths greater than 200 m are counted. The 2-month RMSEs in whole region and western SCS in our concern (13° – 16° N, 110° – 114° E) are shown in Table 3. The assimilation experiments show better performances overall than the Ctrl experiment. Exp1 performed best in SST and SLA but increased the error in salinity forecast. While in situ T/S profile data are

assimilated, the error in salinity forecast can be reduced but the RMSEs in SST and SLA increased slightly at the same time. When the additional Argo trajectory-derived middepth velocities are introduced, the forecast level of other variables is maintained at the previous levels as in Exp2 except slight improvement in SLA. This demonstrates that the method we used can effectively assimilate the Argo trajectory into the model without introducing other problems.

TABLE 3. Two-month-averaged RMSEs between model fields. "Whole" denotes the whole model region (1° – 30° N, 99° – 134° E) where deeper than 200 m; "WSCS" the denotes the western SCS near eastern coast of Vietnam (13° – 16° N, 110° – 113° E).

	Ctrl		Exp1		Exp2		Exp3	
	Whole	WSCS	Whole	WSCS	Whole	WSCS	Whole	WSCS
SST ($^{\circ}$ C)	0.88	1.0	0.26	0.15	0.27	0.19	0.27	0.2
SLA (cm)	8.6	6.6	4.1	2.3	5.1	2.9	4.8	2.7
T ($^{\circ}$ C)	0.86	0.86	0.81	0.92	0.65	0.38	0.65	0.37
S (psu)	0.23	0.06	0.32	0.11	0.17	0.03	0.17	0.04

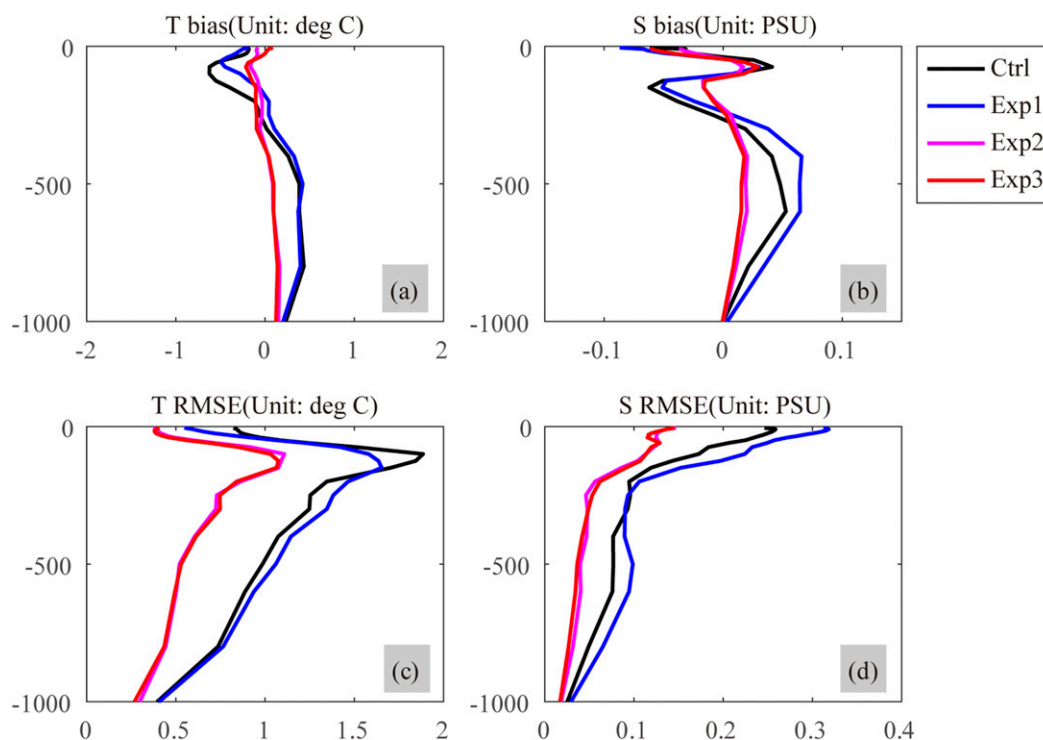


FIG. 13. (a),(b) Mean bias and (c),(d) RMSE of (left) temperature and (right) salinity over 2 months in the whole model region (1° – 30° N, 99° – 134° E) where deeper than 200 m.

The biases of T and S are shown in Fig. 13 (whole model region) and Fig. 14 (western SCS). The assimilation of middepth velocities increased the T and S biases in upper 300 m slightly but reduced the T and S biases below 300 m. The largest biases and RMSEs occurred about 150 m due to the drawback of the model.

Generally, the assimilation of satellite and T/S profile data are not enough to yield accurate modeling of the middepth velocity field in the western SCS. Except for balanced information, assimilation of the Argo trajectory can aid in providing additional unbalanced information, which further improves the forecast quality of the velocity fields at the float parking depth.

5. Summary and discussion

Argo trajectory data are useful in studying basin-scale current structures and detecting subsurface mesoscale eddy in the middle layer of the ocean but are rarely used in ocean data assimilation. In this paper, the Argo trajectory data are assimilated into a regional model of the SCS. Instead of directly assimilating the trajectory data, which requires a complicated trajectory prediction model, the middepth velocities are first retrieved from the float trajectories and then assimilated into the ocean model. As pointed out by Molcard et al. (2005), pseudo-

Lagrangian method is efficient provided that position sampling period is smaller than Lagrangian time scale. In SCS, the sampling period of Argo position is 4 days, while the Lagrangian time scale is about 7–15 days in ocean interior. Thus, this method can be used in SCS to assimilate Argo position into model. Before assimilated into the model, the trajectories were subjected to two rounds of quality control, and the observation error of the middepth velocities was estimated from the distribution of velocity misfits between the Argo and HYCOM-NCODA product and finally set to 2 cm s^{-1} .

Four experiments were designed to evaluate the influence of the Argo trajectory assimilation on the middepth velocity field. A comparison of 2 months of results from four experiments showed that the assimilation of middepth velocities is useful in simulation of the progresses that are not detected from surface, that is, anticyclonic eddy east off Vietnam at $\sim 1200 \text{ m}$. With the introducing of the middepth velocities, the Eulerian velocity are improved for $\sim 11\%$ (zonal) and $\sim 72\%$ (meridional) compared with traditional data assimilation experiment (Exp2); the radius and EC misfit of eddy reduced to 61 and 0.9 km, respectively. Along with the radius decreased, a cold core diameter is narrowed. Except the Eulerian aspect, the Lagrangian velocity is also

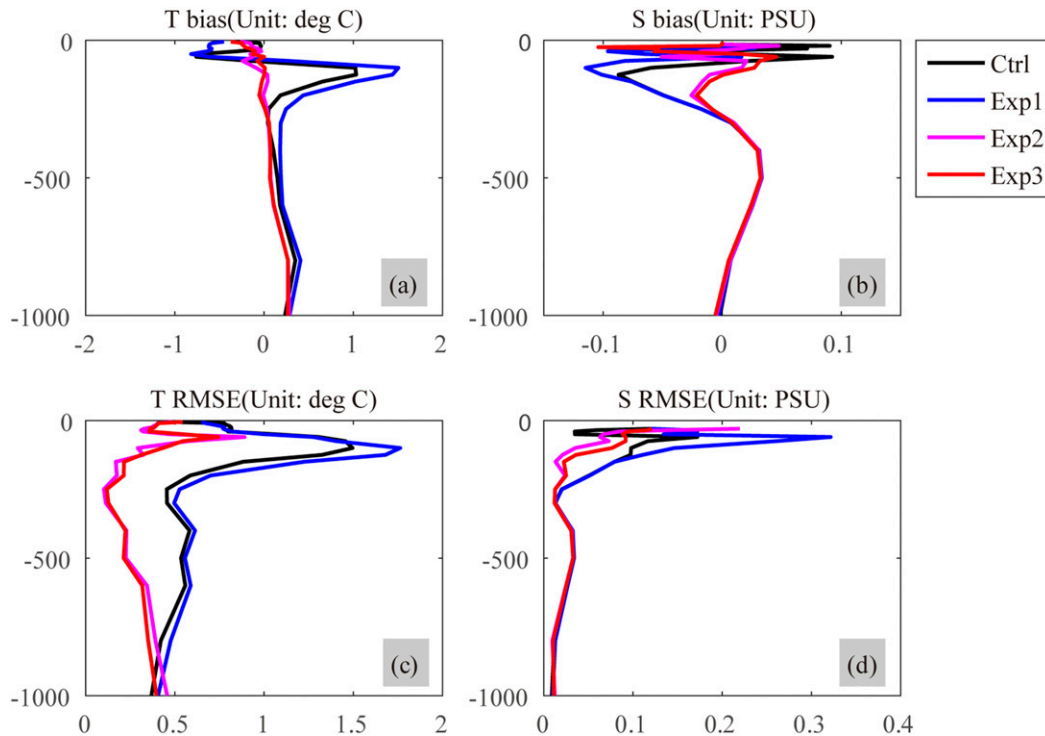


FIG. 14. (a),(b) Mean bias and (c),(d) RMSE of (left) temperature and (right) salinity over 2 months in the western SCS (13° – 16° N, 110° – 114° E).

improved, the predicted trajectory matched well with the realistic trajectory, with an improvement of 7% compared with Exp2. A statistical analysis of the whole region and western SCS showed that this pseudo-Lagrangian assimilation method can reduce the T and S biases and RMSEs below 300 m, and maintain the forecast level of other observations without introducing other problems, such as spurious values in the model states.

The influence of middepth velocity can be seen from the balance relationship. Although the main component of velocity at 1200 m is geostrophic current, accurately modeling the complicated velocity field in the SCS subsurface cannot be adequately accomplished by only adjusting balanced components through satellite and in situ T/S profile data assimilation. Middepth velocity data assimilation can adjust the unbalanced component of velocity field, which influences the properties of the mesoscale process in the subsurface, such as position and strength. Velocity field corrections are not limited to the observation position at the float parking depth but also propagate horizontally and vertically. The vertical influence is weakened with the shallow of depth. As a result, the eddy east of Vietnam tilted southwest with the increase of depth. A comparison of Exp2 and Exp3 showed that the velocity field corrections also impact the mass fields. However, this process is achieved through

model dynamics but not balance relationship, since temperature is the base variable in ROMS IS4DVAR. This probably one reason for the slightly increase of T/S biases and RMSEs in upper 300 m. The above conclusion is mainly drawn from floats 5903457 and 5902163 in the western SCS near Vietnam but can also be applied to other regions with Argo float trajectories in the SCS (not shown). This finding will be useful for more accurately describing the middepth velocity in the SCS and deployment of Argo floats that short cycle period (smaller than Lagrangian time) should be considered for better effect.

Some shortcomings remain in this paper. One is our model does not include tides, which are important for progress in deeper than 2400 m in the SCS (Wang et al. 2016, 2017). The major problem of including tides in model is the changing for assimilating SLA due to its high-frequency variability. Add tides to the model will be considered in future work. The data assimilation system made some simple assumptions as in most ocean data assimilation, including the correlation matrix is isotropic and uniform and observation errors between u and v is uncorrelated, which are not true. The horizontal and vertical correlation length scales are uniform (50 km horizontally and 30 m vertically), which is one reason why the assimilation of satellite data imposed a larger

radius in Exp1 than in the other experiments. The assimilation window is 4 days in the assimilation experiments following Moore et al. (2011b), which may not be the optimal assimilation window in the SCS. These drawbacks will be addressed further in future studies.

Acknowledgments. This study benefitted from the AVISO SLA data (<ftp://ftp-access.aviso.altimetry.fr>), AVHRR SST data (<ftp://eclipse.ncdc.noaa.gov>), EN4.2.1 in situ data (<http://hadobs.metoffice.com/en4/download.html>), Argo trajectory data from Coriolis (<ftp://ftp.ifremer.fr/ifremer/argo>), ERA-Interim dataset from ECMWF (<https://apps.ecmwf.int/datasets/data/interim-full-daily>), CCMP wind data (<ftp://ftp2.remss.com>), SODA3.3.1 data (<https://www.atmos.umd.edu/~ocean/>) and HYCOM-NCODA product (http://tds.hycom.org/thredds/dodsC/GLBu0.08/exp_90.9). This study was jointly supported by the National Key R&D Program of China (2018YFC1406202) and National Natural Science Foundation of China (41675097, 41830964).

REFERENCES

- Atlas, R., R. N. Hoffman, J. Ardizzone, S. M. Leidner, J. C. Jusem, D. K. Smith, and D. Gombos, 2011: A cross-calibrated, multiplatform ocean surface wind velocity product for meteorological and oceanographic applications. *Bull. Amer. Meteor. Soc.*, **92**, 157–174, <https://doi.org/10.1175/2010BAMS2946.1>.
- Carton, J. A., G. A. Chepurin, and L. Chen, 2018: SODA3: A new ocean climate reanalysis. *J. Climate*, **31**, 6967–6983, <https://doi.org/10.1175/JCLI-D-18-0149.1>.
- Castellari, S., A. Griffa, T. M. Özgökmen, and P. M. Poulain, 2001: Prediction of particle trajectories in the Adriatic Sea using Lagrangian data assimilation. *J. Mar. Syst.*, **29**, 33–50, [https://doi.org/10.1016/S0924-7963\(01\)00008-2](https://doi.org/10.1016/S0924-7963(01)00008-2).
- Chao, S. Y., P. T. Shaw, and S. Y. Wu, 1996: Deep water ventilation in the South China Sea. *Deep-Sea Res. I*, **43**, 445–466, [https://doi.org/10.1016/0967-0637\(96\)00025-8](https://doi.org/10.1016/0967-0637(96)00025-8).
- Chen, G., Y. Hou, and X. Chu, 2011: Mesoscale eddies in the South China Sea: Mean properties, spatiotemporal variability, and impact on thermohaline structure. *J. Geophys. Res.*, **116**, C06018, <https://doi.org/10.1029/2010JC006716>.
- , and Coauthors, 2015: Observed deep energetic eddies by seamount wake. *Sci. Rep.*, **5**, 17416, <https://doi.org/10.1038/srep17416>.
- Chu, P. C., and R. Li, 2000: South China Sea isopycnal-surface circulation. *J. Phys. Oceanogr.*, **30**, 2419–2438, [https://doi.org/10.1175/1520-0485\(2000\)030<2419:SCSISC>2.0.CO;2](https://doi.org/10.1175/1520-0485(2000)030<2419:SCSISC>2.0.CO;2).
- Dee, D. P., and Coauthors, 2011: The ERA-Interim reanalysis: Configuration and performance of the data assimilation system. *Quart. J. Roy. Meteor. Soc.*, **137**, 553–597, <https://doi.org/10.1002/qj.828>.
- Fang, G., G. Wang, Y. Fang, and W. Fang, 2012: A review on the South China Sea western boundary current. *Acta Oceanol. Sin.*, **31** (5), 1–10, <https://doi.org/10.1007/s13131-012-0231-y>.
- Good, S. A., M. J. Martin, and N. A. Rayner, 2013: EN4: Quality controlled ocean temperature and salinity profiles and monthly objective analyses with uncertainty estimates. *J. Geophys. Res. Oceans*, **118**, 6704–6716, <https://doi.org/10.1002/2013JC009067>.
- Hu, J., H. Kawamura, H. Hong, and Y. Qi, 2000: A review on the currents in the South China Sea: Seasonal circulation, South China Sea warm current and Kuroshio intrusion. *J. Oceanogr.*, **56**, 607–624, <https://doi.org/10.1023/A:101117531252>.
- Kuznetsov, L. V., K. Ide, and C. K. Jones, 2003: A method for assimilation of Lagrangian data. *Mon. Wea. Rev.*, **131**, 2247–2260, [https://doi.org/10.1175/1520-0493\(2003\)131<2247:AMFAOL>2.0.CO;2](https://doi.org/10.1175/1520-0493(2003)131<2247:AMFAOL>2.0.CO;2).
- Lebedev, K. V., H. Yoshinari, N. A. Maximenko, and P. W. Hacker, 2007: Velocity data assessed from trajectories of Argo floats at parking level and at the sea surface. IPRC Tech. Note 4, 16 pp.
- Li, J., R. Zhang, and B. Jin, 2011: Eddy characteristics in the northern South China Sea as inferred from Lagrangian drifter data. *Ocean Sci.*, **7**, 661–669, <https://doi.org/10.5194/os-7-661-2011>.
- Liao, G., Y. Yuan, and X. Xu, 2005: The three dimensional structure of the circulation in the South China Sea during the winter of 1998 (in Chinese). *Acta Oceanol. Sin.*, **27**, 8–17.
- Lin, X., C. Dong, D. Chen, Y. Liu, J. Yang, B. Zou, and Y. Guan, 2015: Three-dimensional properties of mesoscale eddies in the South China Sea based on eddy-resolving model output. *Deep-Sea Res. I*, **99**, 46–64, <https://doi.org/10.1016/j.dsr.2015.01.007>.
- Liu, Q., A. Kaneko, and J. Su, 2008: Recent progress in studies of the South China Sea circulation. *J. Oceanogr.*, **64**, 753–762, <https://doi.org/10.1007/s10872-008-0063-8>.
- Markova, N. V., and A. V. Bagaev, 2016: The Black Sea Deep Current velocities estimated from the data of Argo profiling floats. *Phys. Oceanogr.*, **3**, <https://doi.org/10.22449/1573-160X-2016-3-23-35>.
- Molcard, A., L. I. Piterbarg, A. Griffa, T. M. Özgökmen, and A. J. Mariano, 2003: Assimilation of drifter observations for the reconstruction of the Eulerian circulation field. *J. Geophys. Res.*, **108**, 3056, <https://doi.org/10.1029/2001JC001240>.
- , A. Griffa, and T. M. Özgökmen, 2005: Lagrangian data assimilation in multilayer primitive equation ocean models. *J. Atmos. Oceanic Technol.*, **22**, 70–83, <https://doi.org/10.1175/JTECH-1686.1>.
- Moore, A. M., H. G. Arango, G. Broquet, B. S. Powell, A. T. Weaver, and J. Zavala-Garay, 2011a: The Regional Ocean Modeling System (ROMS) 4-dimensional variational data assimilation systems: Part I—System overview and formulation. *Prog. Oceanogr.*, **91**, 34–49, <https://doi.org/10.1016/j.pocean.2011.05.004>.
- , and Coauthors, 2011b: The Regional Ocean Modeling System (ROMS) 4-dimensional variational data assimilation systems: Part II—Performance and application to the California Current System. *Prog. Oceanogr.*, **91**, 50–73, <https://doi.org/10.1016/j.pocean.2011.05.003>.
- Muscarella, P., M. Carrier, H. Ngodock, S. Smith, B. L. Lipphardt, A. D. Kirwan, and H. S. Huntley, 2015: Do assimilated drifter velocities improve Lagrangian predictability in an operational ocean model. *Mon. Wea. Rev.*, **143**, 1822–1832, <https://doi.org/10.1175/MWR-D-14-00164.1>.
- Nilsson, J. A. U., S. Dobricic, N. Pinardi, V. Taillandier, and P.-M. Poulain, 2011: On the assessment of Argo float trajectory assimilation in the Mediterranean Forecasting System. *Ocean Dyn.*, **61**, 1475–1490, <https://doi.org/10.1007/s10236-011-0437-0>.
- , —, —, P.-M. Poulain, and D. Pettenuzzo, 2012: Variational assimilation of Lagrangian trajectories in the Mediterranean

- ocean Forecasting System. *Ocean Sci.*, **8**, 249–259, <https://doi.org/10.5194/os-8-249-2012>.
- Ollitrault, M., and J. P. Rannou, 2013: ANDRO: An Argo-based deep displacement dataset. *J. Atmos. Oceanic Technol.*, **30**, 759–788, <https://doi.org/10.1175/JTECH-D-12-00073.1>.
- , and A. Colin de Verdière, 2014: The ocean general circulation near 1000-m depth. *J. Phys. Oceanogr.*, **44**, 384–409, <https://doi.org/10.1175/JPO-D-13-030.1>.
- Park, J. J., and K. Kim, 2013: 2013: Deep currents obtained from Argo float trajectories in the Japan/East Sea. *Deep-Sea Res. II*, **85**, 169–181, <https://doi.org/10.1016/j.dsr2.2012.07.032>.
- , —, and W. R. Crawford, 2004: Inertial currents estimated from surface trajectories of Argo floats. *Geophys. Res. Lett.*, **31**, L13307, <https://doi.org/10.1029/2004GL020191>.
- , —, B. A. King, and S. C. Riser, 2005: An advanced method to estimate deep currents from profiling floats. *J. Atmos. Oceanic Technol.*, **22**, 1294–1304, <https://doi.org/10.1175/JTECH1748.1>.
- Quan, Q., H. Xue, H. Qin, X. Zeng, and S. Peng, 2016: Features and variability of the South China Sea western boundary current from 1992 to 2011. *Ocean Dyn.*, **66**, 795–810, <https://doi.org/10.1007/s10236-016-0951-1>.
- Reynolds, R. W., T. M. Smith, C. Liu, D. B. Chelton, K. S. Casey, and M. G. Schlax, 2007: Daily high-resolution-blended analyses for sea surface temperature. *J. Climate*, **20**, 5473–5496, <https://doi.org/10.1175/2007JCLI1824.1>.
- Slivinski, L., E. T. Spiller, A. Apte, and B. Sandstede, 2015: A hybrid particle–ensemble Kalman filter for Lagrangian data assimilation. *Mon. Wea. Rev.*, **143**, 195–211, <https://doi.org/10.1175/MWR-D-14-00051.1>.
- Song, B., H. Wang, C. Chen, R. Zhang, and S. Bao, 2019: Observed subsurface eddies near the Vietnam coast of the South China Sea. *Acta Oceanol. Sin.*, **38**, 39–46, <https://doi.org/10.1007/s13131-019-1412-8>.
- Spiller, E., A. Budhiraja, K. Ide, and C. Jones, 2008: Modified particle filter methods for assimilating Lagrangian data into a point-vortex model. *Physica D*, **237**, 1498–1506, <https://doi.org/10.1016/j.physd.2008.03.023>.
- Taillandier, V., and A. Griffa, 2006: Implementation of position assimilation for Argo floats in a realistic Mediterranean Sea OPA model and twin experiment testing. *Ocean Sci.*, **3**, 255–289, <https://doi.org/10.5194/os-2-223-2006>.
- , —, P. M. Poulain, and K. Béranger, 2006: Assimilation of Argo float positions in the north western Mediterranean Sea and impact on ocean circulation simulations. *Geophys. Res. Lett.*, **33**, L11604, <https://doi.org/10.1029/2005GL025552>.
- Voet, G., D. Quadfasel, K. A. Mork, and H. Sjøland, 2010: The mid-depth circulation of the Nordic Seas derived from profiling float observations. *Tellus*, **62A**, 516–529, <https://doi.org/10.1111/j.1600-0870.2010.00444.x>.
- Wang, D., and Coauthors, 2013: Progress of regional oceanography study associated with western boundary current in the South China Sea. *Chin. Sci. Bull.*, **58**, 1205–1215, <https://doi.org/10.1007/s11434-012-5663-4>.
- Wang, G., J. Su, and P. C. Chu, 2003: Mesoscale eddies in the South China Sea observed with altimeter data. *Geophys. Res. Lett.*, **30**, 2121, <https://doi.org/10.1029/2003GL018532>.
- Wang, H., G. Wang, D. Chen, and R. Zhang, 2012a: Reconstruction of three-dimensional Pacific temperature with Argo and satellite observations. *Atmos.–Ocean*, **50** (Suppl.), 116–128, <https://doi.org/10.1080/07055900.2012.742421>.
- , R. Zhang, G. Wang, Y. An, and B. Jin, 2012b: Quality control of Argo temperature and salinity observation profiles (in Chinese). *Chin. J. Geophys.*, **55**, 577–588.
- Wang, X., S. Peng, Z. Liu, R. Huang, Y. Qian, and Y. Li, 2016: Tidal mixing in the South China Sea: An estimate based on the internal tide energetics. *J. Phys. Oceanogr.*, **46**, 107–124, <https://doi.org/10.1175/JPO-D-15-0082.1>.
- , Z. Liu, and S. Peng, 2017: Impact of tidal mixing on water mass transformation and circulation in the South China Sea. *J. Phys. Oceanogr.*, **47**, 419–432, <https://doi.org/10.1175/JPO-D-16-0171.1>.
- , W. Zhang, P. Wang, J. Yang, and H. Wang, 2018: Research on mid-depth current of basin scale in the South China Sea based on historical Argo observations (in Chinese). *Haiyang Xuebao*, **40**, 1–14.
- Warner, J. C., C. R. Sherwood, H. G. Arango, and R. P. Signell, 2005: Performance of four turbulence closure models implemented using a generic length scale method. *Ocean Modell.*, **8**, 81–113, <https://doi.org/10.1016/j.ocemod.2003.12.003>.
- Weaver, A. T., C. Deltel, É. Machu, S. Ricci, and N. Daget, 2005: A multivariate balance operator for variational ocean data assimilation. *Quart. J. Roy. Meteor. Soc.*, **131**, 3605–3625, <https://doi.org/10.1256/qj.05.119>.
- Wyrtki, K., 1961: Physical oceanography of the Southeast Asian waters. Scripps Institution of Oceanography Rep., 195 pp., <https://escholarship.org/uc/item/49n9x3t4>.
- Xie, J., and J. Zhu, 2008: Estimation of the surface and mid-depth currents from Argo floats in the Pacific and error analysis. *J. Mar. Syst.*, **73**, 61–75, <https://doi.org/10.1016/j.jmarsys.2007.09.001>.
- , F. Counillon, J. Zhu, and L. Bertino, 2011: An eddy resolving tidal-driven model of the South China Sea assimilating along-track SLA data using the EnOI. *Ocean Sci.*, **7**, 609–627, <https://doi.org/10.5194/os-7-609-2011>.
- Xiu, P., F. Chai, L. Shi, H. Xue, and Y. Chao, 2010: A census of eddy activities in the South China Sea during 1993–2007. *J. Geophys. Res.*, **115**, C03012, <https://doi.org/10.1029/2009JC005657>.
- Yuan, D., 2012: A numerical study of the South China Sea deep circulation and its relation to the Luzon Strait transport. *Acta Oceanol. Sin.*, **21**, 187–202.
- Zhang, Z., F. Qiao, and J. Guo, 2014: Subsurface eddies in the southern South China Sea detected from in-situ observation in October 2011. *Deep-Sea Res. I*, **87**, 30–34, <https://doi.org/10.1016/j.dsr.2014.02.004>.
- Zhang, Z., J. Tian, B. Qiu, W. Zhao, P. Chang, D. Wu, and X. Wan, 2016: Observed 3D structure, generation, and dissipation of oceanic mesoscale eddies in the South China Sea. *Sci. Rep.*, **6**, 24349, <https://doi.org/10.1038/srep24349>.
- Zhou, H., D. Yuan, R. Li, and L. He, 2010: The western South China Sea currents from measurements by Argo profiling floats during October to December 2007. *Chin. J. Oceanol. Limnol.*, **28**, 398–406, <https://doi.org/10.1007/s00343-010-9052-z>.